nature

https://doi.org/10.1038/s41586-023-06006-7

Accelerated Article Preview

Suppressed phase segregation for triple-junction perovskite solar cells

Received: 30 October 2022

Accepted: 23 March 2023

Accelerated Article Preview

Cite this article as: Wang, Z. et al. Suppressed phase segregation for triple-junction perovskite solar cells. *Nature* https://doi.org/10.1038/s41586-023-06006-7 (2023)

Zaiwei Wang, Lewei Zeng, Tong Zhu, Hao Chen, Bin Chen, Dominik J. Kubicki, Adam Balvanz, Chongwen Li, Aidan Maxwell, Esma Ugur, Roberto dos Reis, Matthew Cheng, Guang Yang, Biwas Subedi, Deying Luo, Juntao Hu, Junke Wang, Sam Teale, Suhas Mahesh, Sasa Wang, Shuangyan Hu, Euidae Jung, Mingyang Wei, So Min Park, Luke Grater, Erkan Aydin, Zhaoning Song, Nikolas J. Podraza, Zheng-Hong Lu, Jinsong Huang, Vinayak P. Dravid, Stefaan De Wolf, Yanfa Yan, Michael Grätzel, Mercouri Kanatzidis & Edward Sargent

Suppressed phase segregation for triple-junction perovskite solar cells

Authors: Zaiwei Wang[1†], Lewei Zeng[1†], Tong Zhu[1†], Hao Chen[1†], Bin Chen[1,2], Dominik J. Kubicki[3], Adam Balvanz[2], Chongwen Li[1,4], Aidan Maxwell[1], Esma Ugur[5], Roberto dos Reis[6], Matthew Cheng[6], Guang Yang[7], Biwas Subedi[4], Deying Luo[8], Juntao Hu[9], Junke Wang[1], Sam Teale[1], Suhas Mahesh[1], Sasa Wang[1], Shuangyan Hu[1], Euidae Jung[1], Mingyang Wei[1,10], So Min Park[1], Luke Grater[1], Erkan Aydin[5], Zhaoning Song[4], Nikolas J. Podraza[4], Zheng-Hong Lu[8,9], Jinsong Huang[7], Vinayak P Dravid[6], Stefaan De Wolf[5], Yanfa Yan[4], Michael Grätzel[10], Mercouri Kanatzidis[2], Edward Sargent[1,2,11*]

Affiliations:

[1]Department of Electrical and Computer Engineering, University of Toronto, 35 St George Street, Toronto, Ontario M5S 1A4, Canada.

[2]Department of Chemistry, Northwestern University, Evanston, Illinois 60208, United States.

[3]Department of Physics, University of Warwick, Coventry CV4 7AL, United Kingdom.

[4]Department of Physics and Astronomy and Wright Center for Photovoltaics Innovation and Commercialization, The University of Toledo, Toledo, Ohio 43606, United States.

[5]KAUST Solar Center (KSC), Physical Sciences and Engineering Division (PSE), King Abdullah University of Science and Technology (KAUST), Thuwal 23955-6900, Kingdom of Saudi Arabia.

[6]Department of Materials Science and Engineering, Northwestern University, Evanston, Illinois 60208, United States.

[7]Department of Applied Physical Sciences, University of North Carolina at Chapel Hill, Chapel Hill, North Carolina 27599, United States.

[8]Department of Materials Science and Engineering, University of Toronto, Toronto, Ontario M5G 3E4, Canada.

[9]Department of Physics, Center for Optoelectronics Engineering Research, Yunnan University, Kunming 650091, China.

[10] Laboratory of Photonics and Interfaces, Institute of Chemical Sciences and Engineering, Ecole Polytechnique Fedérale de Lausanne (EPFL), CH-1015 Lausanne, Switzerland.

[11]Department of Electrical and Computer Engineering, Northwestern University, Evanston, Illinois 60208, United States.

†These authors contribute equally to this work.

*Correspondence: ted.sargent@utoronto.ca

Abstract:

The tunable band gaps and facile fabrication of perovskites make them attractive for multi-junction photovoltaics[1,2]. However, light-induced phase segregation limits their efficiency and stability[3-5]: this occurs in wide band gap (> 1.65 eV) I/Br mixed perovskite absorbers, and becomes even more acute in the top cells of triple-junction solar photovoltaics that requires a fully 2.0 eV band gap absorber[2,6]. We report herein that lattice distortion in I/Br mixed perovskites is correlated with the suppression of phase segregation, generating an increased ion migration energy barrier arising from the decreased average interatomic distance between A-site cation and iodide. Using a ~2.0 eV Rb/Cs mixed-cation inorganic perovskite with large lattice distortion in the top subcell, we fabricated all-perovskite triple-junction solar cells and achieved an efficiency of 24.3% (23.3% certified quasi-steady-state efficiency) with an open-circuit voltage of 3.21 V. This is, to our knowledge, the first reported certified efficiency for perovskite-based triple-junction solar cells. The triple-junction devices retain 80% of their initial efficiency following 420 hours of operation at the maximum power point.

Multi-junction solar cells offer routes to increase power conversion efficiency (PCE) by stacking multiple light-absorbing layers with complementary band gaps and minimizing charge-carrier thermalization losses[7,8]. Halide perovskites with tunable band gaps, long charge carrier diffusion lengths, high light-harvesting efficiency and facile fabrication are compelling materials for multi-junction photovoltaics[1,2,9-14]. However, the challenge of light-induced phase segregation (LIPS) for wide band gap (> 1.65 eV) I/Br mixed perovskite absorbers in top subcells limits the PCE and stability of perovskite-based multi-junction photovoltaics, especially triple-junction solar cells (TJSCs)[2-4,6,15]. Perovskite-based TJSCs such as the all-perovskite, perovskite/perovskite/Si and perovskite/perovskite/CuInGa(Se,S) have a higher theoretical PCE than their double- and single-junction counterparts[2,16]. Nevertheless, to date, perovskite-based TJSCs have only achieved an efficiency of 20.1%, a PCE that decreases to ~5% after 1 hour of continuous operation. (**Supplementary Table 1**)[6,17-19].

We noted that most previously reported I/Br mixed perovskite compositions exhibiting suppressed LIPS have enlarged lattice distortions: these have been achieved via doping with smaller A-site cations, and also by increasing the larger X-site iodide anion content[3,4,20-26]. Based on this observation, we hypothesized that increasing lattice distortion raises the ion migration energy barrier, thereby suppressing LIPS (**Fig. 1a**). For a similar range of band gaps, Cs-based inorganic perovskites, with the smaller A-site cation and the higher iodide anion content, have a higher degree of lattice distortion and better stability under illumination than organic-inorganic hybrid perovskites[1,27,28].

However, 2.0 eV band gap Cs-based inorganic perovskites, such as $CsPbI_{1.4}Br_{1.6}$ (**Supplementary Fig. 1**), as the absorber in the top subcell for perovskite-based TJSCs, still face the challenge of LIPS under illumination[22].

We find that Rb, with a smaller cation radius than Cs, can be doped into the inorganic perovskite lattice and that the upper limit of Rb doping content is positively correlated with Br content. Rb^+ lattice-doping widens the band gap of inorganic perovskites, meaning Rb/Cs solid solutions require a higher I content to achieve a band gap of ~2.0 eV (such as $Rb_{0.15}Cs_{0.85}PbI_{1.75}Br_{1.25}$, compared to ~2.0 eV $CsPbI_{1.4}Br_{1.6}$). The ~2.0 eV Rb/Cs mixed-cation inorganic perovskites with a larger degree of lattice distortion than their Cs-based counterparts show suppressed LIPS because of the decreased average interatomic distance of the A-site cation (A = Cs or Rb) and iodide (I), and the increased energy barrier of halide ion migration. Finally, we applied the ~2.0 eV Rb/Cs perovskites in all-perovskite TJSCs and achieved an efficiency of 24.3% (23.29% certified quasi-steady-state efficiency). Our all-perovskite TJSC retains 80% of its initial efficiency after 420 hours of operation at maximum power point under room temperature and AM1.5G 1-sun illumination.

Rb/Cs mixed-cation inorganic perovskites

We partially replaced Cs^+ with Rb^+ in a Cs-based I/Br mixed inorganic perovskite $CsPbI_{1.75}Br_{1.25}$. Ultraviolet-visible (UV-Vis) absorption spectra (**Fig. 1b** and **Supplementary Fig. 2**) show a gradual blue-shift of the absorption edge from 631 nm for the pure Cs-based perovskite $CsPbI_{1.75}Br_{1.25}$ to 614 nm for the Rb/Cs mixed-cation perovskite $Rb_{0.2}Cs_{0.8}PbI_{1.75}Br_{1.25}$. From X-ray diffraction (XRD), we find that Rb can

be doped into the $CsPbI_{1.75}Br_{1.25}$ lattice to form a pure perovskite phase in $Rb_xCs_{1-x}PbI_{1.75}Br_{1.25}$ ($x \leq 0.2$) films (**Fig. 1c** and **Supplementary Fig. 2**). For pure-halide Rb/Cs mixed-cation films, $Rb_xCs_{1-x}PbBr_3$ ($x \leq 0.7$) and $Rb_xCs_{1-x}PbI_3$ ($x \leq 0.1$) are pure perovskite phases (**Supplementary Note 1** for a detailed discussion). Thus, the upper limit of Rb lattice-doping content for retaining a pure perovskite phase is positively correlated with the Br content in these Rb/Cs mixed-cation materials.

Solid-state nuclear magnetic resonance (NMR) spectroscopy is used to study dopants in halide perovskites[29,30]. We carried out solid-state magic angle spinning (MAS) NMR measurements on materials prepared by mechanosynthesis to study the local structure of ^{133}Cs and ^{87}Rb. Upon Rb^+ doping of single-halide and mixed-halide inorganic perovskites, the ^{133}Cs perovskite peaks broaden and shift to higher frequencies. The ^{87}Rb spectra show peaks corresponding to Rb^+ inside the perovskite phase. These observations corroborate that Rb^+ can be incorporated into Cs-based inorganic perovskites (**Fig. 1d**, and **Supplementary Fig. 3-5. Supplementary Note 2 and 3** for a detailed discussion)[29].

Rb/Cs mixed-cation perovskites with a band gap near 2.0 eV (**Supplementary Fig. 6**, **Supplementary Table 2-4**) including $Rb_xCs_{1-x}PbI_2Br$ (x= 0, 0.05, 0.1, 0.15, 0.2), $Rb_xCs_{1-x}PbI_{1.75}Br_{1.25}$ (x=0, 0.05, 0.1, 0.15, 0.2, 0.25), and $Rb_xCs_{1-x}PbI_{1.5}Br_{1.5}$ (x=0, 0.1, 0.15, 0.2, 0.25, 0.3) were employed as the absorbers in PSCs. Devices with perovskite absorbers of x = 0.1 in $Rb_xCs_{1-x}PbI_2Br$, x = 0.15 in $Rb_xCs_{1-x}PbI_{1.75}Br_{1.25}$ and x = 0.2 in $Rb_xCs_{1-x}PbI_{1.5}Br_{1.5}$ demonstrate the highest open-current voltage (V_{OC}) (**Fig. 1e** and **Supplementary Table 2-4**). Among the various absorber compositions,

$Rb_{0.15}Cs_{0.85}PbI_{1.75}Br_{1.25}$ has a band gap of ~2.0 eV (**Supplementary Table 3**) and delivers the highest V_{OC} in PSCs compared to other Rb-doped inorganic perovskites with band gap ≤ 2.0 eV (**Supplementary Table 2-4**). We therefore employed $Rb_{0.15}Cs_{0.85}PbI_{1.75}Br_{1.25}$ as our target ~2.0 eV Rb/Cs mixed-cation perovskite sample in the following context. We also chose a Cs-based perovskite $CsPbI_{1.4}Br_{1.6}$ with the same ~2.0 eV band gap and a Cs-based perovskite $CsPbI_{1.75}Br_{1.25}$ with the same I/Br ratio as control samples compared to the target sample.

The top-view scanning electron microscopy (SEM) images in **Supplementary Fig. 7** show that the $CsPbI_{1.4}Br_{1.6}$, $CsPbI_{1.75}Br_{1.25}$ and $Rb_{0.15}Cs_{0.85}PbI_{1.75}Br_{1.25}$ perovskite films are uniform and pinhole-free. These films also have a low root mean square (RMS) roughness (< 26 nm), as shown in atomic force microscopy (AFM) images (**Supplementary Fig. 7**). The energy-dispersive X-ray spectroscopy (EDX) mapping and depth profile X-ray photoelectron spectroscopy (XPS) of $Rb_{0.15}Cs_{0.85}PbI_{1.75}Br_{1.25}$ films (**Supplementary Fig. 8-10**) show a uniform distribution of Rb at the surface and throughout the depth of the perovskite films.–

Density functional theory (DFT) calculations reveal a deeper Helmholtz free energy (larger thermodynamic driving force) for Rb/Cs mixed-cation perovskites with an increase in Br content (**Fig. 1f**). Additionally, Rb content is also correlated with the phase stability (**Supplementary Fig. 4 and 5**. **Supplementary Note 2** for a detailed discussion)[31]. Thus, we attribute the positive correlation between the upper limit of Rb doping content and the Br content in inorganic perovskites to the increase in

thermodynamic driving force and the relatively stable perovskite phase in Br-rich perovskites.

Suppressed LIPS

We carried out time-dependent photoluminescence (PL) measurements of encapsulated $CsPbI_{1.4}Br_{1.6}$, $CsPbI_{1.75}Br_{1.25}$ and $Rb_{0.15}Cs_{0.85}PbI_{1.75}Br_{1.25}$ perovskite films under 1-sun illumination (AM 1.5G). The initial PL spectrum of $CsPbI_{1.4}Br_{1.6}$ shows a PL peak at 610 nm (**Fig. 2a**). A new lower-energy PL peak at ~680 nm appears after 10 minutes due to LIPS. With the extension of illumination time, the intensity of the peak at ~680 nm increases, and simultaneously the initial peak at ~610 nm decreases in intensity. The initial PL peak of the $CsPbI_{1.75}Br_{1.25}$ film is at 630 nm, and a lower-energy PL peak at ~680 nm appears after 30 minutes of illumination (**Fig. 2b**). After 60 minutes of illumination, the $CsPbI_{1.75}Br_{1.25}$ film shows a lower PL intensity of the peak at ~680 nm than the $CsPbI_{1.4}Br_{1.6}$ film. Our target sample, $Rb_{0.15}Cs_{0.85}PbI_{1.75}Br_{1.25}$, which exhibits an initial PL peak at ~ 616 nm, shows a negligible peak shift (less than 2 nm) and an absence of a lower-energy peak after 60-minute illumination (**Fig. 2c**). These results indicate that the $CsPbI_{1.75}Br_{1.25}$ films with a higher iodide content undergoe weaker LIPS than do $CsPbI_{1.4}Br_{1.6}$ films, and that ~2.0 eV Rb/Cs mixed-cation perovskites show the best light stability among these. The spatial homogeneity of the PL peak position agrees with this finding (**Supplementary Fig. 11**).–

To study the mechanism of LIPS suppression in Rb/Cs mixed-cation perovskites, we grew single crystals in solid-state reactions with the loading compositions $CsPbI_{1.4}Br_{1.6}$, $CsPbI_{1.75}Br_{1.25}$, and $Rb_{0.15}Cs_{0.85}PbI_{1.75}Br_{1.25}$, and analyzed their single crystal diffraction

data. All compounds crystallize in a monoclinic crystal system best described by the $P2_1/m$ space group (**Fig. 2d**, **e, Supplementary Fig. 12-14** and **Supplementary Table 5**. **Supplementary Note 4** and **5** for a detailed discussion). These structures exist as a supercell (**Supplementary Fig. 12**. **Supplementary Note 4** for a detailed discussion), presumably because of the partial ordering of the halides. To the best of our knowledge, this has not yet been reported in the literature. The single crystal XRD data unambiguously show that Rb substitutes Cs on the A-site.

Substituting Rb at the Cs site leads to increased lattice distortions as evidenced by the decrease in the Pb–X–Pb (where X = I/Br mixed sites) bond angles (∠Pb–X–Pb) and the widening of the band gap when comparing $Rb_{0.15}Cs_{0.85}PbI_{1.75}Br_{1.25}$ versus $CsPbI_{1.75}Br_{1.25}$ (**Supplementary Fig. 15**, **Supplementary Table 6** and **7**)[32,33]. The Pb–X–Pb angles in $CsPbI_{1.75}Br_{1.25}$ show a slight increasing distortion compared to those of $CsPbI_{1.4}Br_{1.6}$ (**Supplementary Table 7**. **Supplementary Note 6** and **7** for a detailed discussion).

We further estimated the concentration of mobile ions using a mobile ion charging-discharging method that has demonstrated consistency with ion migration energy barriers[34,35]. The typical transient currents in devices are shown in **Fig. 2f** and the calculated average mobile ion concentrations are summarized in **Fig. 2g**. The mobile ion concentrations decrease from 1.45×10^{17} cm^{-3} for the $CsPbI_{1.4}Br_{1.6}$ device to 1.01×10^{17} cm for the $CsPbI_{1.75}Br_{1.25}$ device and 7.89×10^{16} cm^{-3} for the $Rb_{0.15}Cs_{0.85}PbI_{1.75}Br_{1.25}$ device.

188 To explore further the distortion of the I or Br sites, we analyzed the DFT-relaxed
189 structures of $CsPbI_{1.4}Br_{1.6}$, $CsPbI_{1.75}Br_{1.25}$, and $Rb_{0.15}Cs_{0.85}PbI_{1.75}Br_{1.25}$. The average ∠
190 Pb–I–Pb decreases from 143.54° for $CsPbI_{1.4}Br_{1.6}$ to 143.06° for $CsPbI_{1.75}Br_{1.25}$ and
191 then decreases further to 143.05° for I far away from Rb and 142.39° for I close to Rb
192 in $Rb_{0.15}Cs_{0.85}PbI_{1.75}Br_{1.25}$, which is indicative of increased distortion of the I site with
193 the introduction of I or Rb (**Fig. 2h** and **Supplementary Fig. 16** and **17**). Lattice
194 distortion results in a large variation for interatomic distances of A-site cation and X-
195 site anion (A···X) compared to Pb···X interatomic distances (**Supplementary Table 8**
196 and **9**). Thus, we mainly focus on discussing the A···X interatomic distances in the text.
197 The average Cs···I interatomic distance decreases from 4.04 Å for $CsPbI_{1.4}Br_{1.6}$ to 4.02
198 Å for $CsPbI_{1.75}Br_{1.25}$. For $Rb_{0.15}Cs_{0.85}PbI_{1.75}Br_{1.25}$, the average interatomic distance
199 further decreases to 3.98 Å of Cs and I, and 3.95 Å of Rb and I (**Fig. 2i** and
200 **Supplementary Fig. 17**). The energy barrier of I migrating to an I vacancy (V_I)
201 increases from 0.33 eV for $CsPbI_{1.4}Br_{1.6}$ to 0.40 eV for $CsPbI_{1.75}Br_{1.25}$ (**Fig. 2j** and
202 **Supplementary Fig. 18 and 19**). Additionally, the migration energy barriers for
203 $Rb_{0.15}Cs_{0.85}PbI_{1.75}Br_{1.25}$ are further increased to 0.42 eV for V_I far from Rb and 0.51 eV
204 for V_I close to Rb.

205 The average A···I interatomic distance is longer than that of A···Br, and the migration
206 energy barrier of I to V_I is the lowest among all four studied ion migration transitions
207 (**Fig. 2i** and **2j**). In addition, the defect formation energy of V_I is lower than that of V_{Br}
208 based on our calculations (**Supplementary Fig. 20**). Thus, the migration energy
209 barriers of these materials are dominated by that of I to V_I and increase with the

introduction of I and Rb. This also indicates that the most mobile ions arise from I to V_I migration, consistent with previous reports[34].

Thus, we conclude that increasing the lattice distortion in I/Br mixed inorganic perovskites increases the I-site distortion. This is associated with a decrease in the average A···I interatomic distance, which enhances the ion migration energy barrier and suppresses ion migration and LIPS. This conclusion also offers a more comprehensive explanation for the reported phenomena of suppressed LIPS (**Supplementary Note 8** for a detailed discussion).

2.0 eV single-junction PSCs

As ~2.0 eV perovskites are ideal absorbers as the top subcells in all-perovskites TJSCs, we compared the performance of ~2.0 eV $CsPbI_{1.4}Br_{1.6}$ and $Rb_{0.15}Cs_{0.85}PbI_{1.75}Br_{1.25}$ devices based on the p-i-n configuration of indium tin oxide (ITO)/NiO_x/[4-(3,6-Dimethyl-9H-carbazol-9-yl)butyl]phosphonic acid (Me-4PACz)/perovskite/phenethylammonium iodide and ethane-1,2-diammonium iodide ($PEAI\text{-}EDAI_2$)/phenyl C61 Butyric Acid Methyl Ester (PCBM)/polyethyleneimine ethoxylated (PEIE)/SnO_x/Ag (**Supplementary Fig. 21**). For the control 2.0 eV $CsPbI_{1.4}Br_{1.6}$ device, the PCE is 12.59% with a V_{OC} of 1.288 V (**Fig. 3a**). The PCE of the $Rb_{0.15}Cs_{0.85}PbI_{1.75}Br_{1.25}$ device increases to 13.41% with a V_{OC} of 1.312 V. Their stabilized power output (SPO) efficiencies are 12.1% and 13.3%, respectively (**Fig. 3b**). A statistical analysis of the photovoltaic parameters of 54 devices demonstrates the reproducibility of high-performance $Rb_{0.15}Cs_{0.85}PbI_{1.75}Br_{1.25}$ devices (**Fig. 3c**). The $Rb_{0.15}Cs_{0.85}PbI_{1.75}Br_{1.25}$ device with suppressed LIPS exhibits improved operational

stability compared to the $CsPbI_{1.4}Br_{1.6}$ device (**Supplementary Fig. 21**. **Supplementary Note 9** for a detailed discussion). The quasi-Fermi level splitting (QFLS) of the partially-complete device stacks (ITO glass/NiO_x/Me-4PACz/perovskites) of these perovskites shows that the $Rb_{0.15}Cs_{0.85}PbI_{1.75}Br_{1.25}$ sample has high QFLS (1.417 ± 0.004 eV) with a narrow spatial distribution in comparison with the $CsPbI_{1.4}Br_{1.6}$ perovskite (1.318 ± 0.054 eV) (**Fig. 3d**), which is indicative of reduced nonradiative recombination[36]. The Urbach energy values obtained from photothermal deflection spectroscopy (PDS) measurements decrease from 45 meV for $CsPbI_{1.4}Br_{1.6}$ to 31 meV for $Rb_{0.15}Cs_{0.85}PbI_{1.75}Br_{1.25}$ perovskite films (**Fig. 3e**). This suggests decreased electronic disorder of $Rb_{0.15}Cs_{0.85}PbI_{1.75}Br_{1.25}$ perovskite films, consistent with suppressed LIPS and improved perovskite film quality (**Supplementary Note 10** for a detailed discussion)[37,38]. These are correlative with the high V_{OC} observed for the $Rb_{0.15}Cs_{0.85}PbI_{1.75}Br_{1.25}$ device[36,37].

All-perovskite triple-junction solar cells

We further employed the ~2.0 eV Rb/Cs mixed-cation inorganic perovskite as the absorber for the top subcell in a monolithic all-perovskite TJSC. The configuration of the TJSC is ITO glass/NiO_x/Me-4PACz/2.0 eV inorganic perovskite (170 nm)/PEAI-$EDAI_2$/PCBM/PEIE/SnO_x/ITO/NiO_x/Me-4PACz/1.6 eV perovskite (780 nm)/PEAI-$EDAI_2$/PCBM/PEIE/SnO_x/Au/PEDOT:PSS/1.22 eV SnPb perovskite (870 nm)/C_{60}/SnO_x/Ag (**Fig. 4a**). **Fig. 4b** shows the *J-V* curves of a champion all-perovskite TJSC. The PCE from the reverse scan is 24.33% with a V_{OC} of 3.215 V, a short-circuit current (J_{SC}) of 9.71 mA/cm^2, and a fill factor (FF) of 77.93%. There is negligible

hysteresis between the forward and reverse *J-V* scans of the device (**Fig. 4b**). We achieved a certified quasi-steady-state (QSS) PCE of 23.29% in an accredited independent PV calibration laboratory (NREL) (**Fig. 4c** and **Supplementary Fig. 22**), which is, to our knowledge, the first reported certified PCE for perovskite-based TJSCs. The SPO efficiency over 20 minites is 24.1% (**Supplementary Fig. 23**). The integrated J_{SC} values for the ~2.0 eV, ~1.6 eV and ~1.22 eV cells from EQE measurements of a TJSC are 10.18, 9.95, and 9.31 mA/cm^2, respectively (**Fig. 4d**). *J-V* performance from 32 devices is detailed in **Supplementary Fig. 24**. The efficiency of all-perovskite TJSCs will further improve via the development of new passivation strategies, improved interfacial contact, and the optimization of light management (**Supplementary Table 11. Supplementary Note 11** for a detailed discussion).

We tracked the PCE of an encapsulated device stored in a nitrogen glovebox. After 120 days, the PCE shows a negligible decline (**Supplementary Fig. 23**). We also monitored the performance of an encapsulated TJSC under maximum power point tracking conditions and continuous AM1.5G one-sun illumination at room temperature in an ambient atmosphere (**Fig. 4e**). The optimized device based on a Rb/Cs mixed-cation perovskite retains 80% of its initial PCE after 420 hours of continuous operation. Further analysis shows that 2.0 eV Rb/Cs perovskites undergo phase segregation after 450 h MPP tracking (**Supplementary Fig. 25, Supplementary Table 12, Supplementary Note 12** for a detailed discussion**)**. These results indicate that, while Rb incorporation offers a promising route to decreased light-induced phase segregation,

the topic will benefit from further study along the path to a long-term operating lifetime solution.

References

1 Stoumpos, C. C., Malliakas, C. D. & Kanatzidis, M. G. Semiconducting tin and lead iodide perovskites with organic cations: Phase transitions, high mobilities, and near-infrared photoluminescent properties. *Inorg. Chem.* **52**, 9019-9038 (2013).

2 Eperon, G. E., Hörantner, M. T. & Snaith, H. J. Metal halide perovskite tandem and multiple-junction photovoltaics. *Nat. Rev. Chem.* **1**, 0095 (2017).

3 Hoke, E. T. *et al.* Reversible photo-induced trap formation in mixed-halide hybrid perovskites for photovoltaics. *Chem. Sci.*, **6**, 613-617 (2015).

4 McMeekin, D. P. *et al.* A mixed-cation lead mixed-halide perovskite absorber for tandem solar cells. *Science* **351**, 151-155 (2016).

5 Abdi-Jalebi, M. *et al.* Maximizing and stabilizing luminescence from halide perovskites with potassium passivation. *Nature* **555**, 497-501 (2018).

6 Xiao, K. *et al.* Solution-processed monolithic all-perovskite triple-junction solar cells with efficiency exceeding 20%. *ACS Energy Lett.* **5**, 2819-2826 (2020).

7 Henry, C. H. Limiting efficiencies of ideal single and multiple energy gap terrestrial solar cells. *J. Appl. Phys.* **51**, 4494-4500 (1980).

8 Shockley, W. & Queisser, H. J. Detailed balance limit of efficiency of p-n junction solar cells. *J. Appl. Phys.* **32**, 510-519 (1961).

9 Pazos-Outon, L. M. *et al.* Photon recycling in lead iodide perovskite solar cells.

Science **351**, 1430-1433 (2016).

10 Laboratory, N. R. E. *Best research-cell efficiencies*, <https://www.nrel.gov/pv/cell-efficiency.html> (2022).

11 Green, M. A. *et al.* Solar cell efficiency tables (Version 60). *Prog. Photovolt. Res. Appl.* **30**, 687-701 (2022).

12 Kojima, A., Teshima, K., Shirai, Y. & Miyasaka, T. Organometal halide perovskites as visible-light sensitizers for photovoltaic cells. *J. Am. Chem. Soc.* **131**, 6050-6051 (2009).

13 Lee, M. M., Teuscher, J., Miyasaka, T., Murakami, T. N. & Snaith, H. J. Efficient hybrid solar cells based on meso-superstructured organometal halide perovskites. *Science* **338**, 643-647 (2012).

14 Kim, H. S. *et al.* Lead iodide perovskite sensitized all-solid-state submicron thin film mesoscopic solar cell with efficiency exceeding 9%. *Sci. Rep.* **2**, 591 (2012).

15 Xu, J. *et al.* Triple-halide wide–band gap perovskites with suppressed phase segregation for efficient tandems. *Science* **367**, 1097 (2020).

16 Hörantner, M. T. *et al.* The potential of multijunction perovskite solar cells. *ACS Energy Lett.* **2**, 2506-2513 (2017).

17 McMeekin, D. P. *et al.* Solution-processed all-perovskite multi-junction solar cells. *Joule* **3**, 387-401 (2019).

18 Wang, J. *et al.* 16.8% Monolithic all-perovskite triple-junction solar cells via a universal two-step solution process. *Nat. Commun.* **11**, 5254 (2020).

19 Zheng, J. *et al.* Monolithic perovskite–perovskite–silicon triple-junction

tandem solar cell with an efficiency of over 20%. *ACS Energy Lett.*, 3003-3005 (2022).

20 Muscarella, L. A. *et al.* Lattice compression increases the activation barrier for phase segregation in mixed-halide perovskites. *ACS Energy Lett.* **5**, 3152-3158 (2020).

21 Rehman, W. *et al.* Photovoltaic mixed-cation lead mixed-halide perovskites: links between crystallinity, photo-stability and electronic properties. *Energy Environ. Sci.* **10**, 361-369 (2017).

22 Beal, R. E. *et al.* Cesium lead halide perovskites with improved stability for tandem solar cells. *J. Phys. Chem. Lett.* **7**, 746-751 (2016).

23 Brennan, M. C., Draguta, S., Kamat, P. V. & Kuno, M. Light-induced anion phase segregation in mixed halide perovskites. *ACS Energy Lett.* **3**, 204-213 (2017).

24 Noh, J. H., Im, S. H., Heo, J. H., Mandal, T. N. & Seok, S. I. Chemical management for colorful, efficient, and stable inorganic-organic hybrid nanostructured solar cells. *Nano Lett.* **13**, 1764-1769 (2013).

25 Yuan, Y. B. & Huang, J. S. Ion migration in organometal trihalide perovskite and its impact on photovoltaic efficiency and stability. *Acc. Chem. Res.* **49**, 286-293 (2016).

26 Beal, R. E. *et al.* Structural origins of light-induced phase segregation in organic-inorganic halide perovskite photovoltaic Materials. *Matter* **2**, 207-219 (2020).

27 Marronnier, A. *et al.* Anharmonicity and disorder in the black phases of cesium lead iodide used for stable inorganic perovskite solar cells. *ACS Nano* **12**, 3477-3486 (2018).

28 Zhou, W. *et al.* Light-independent ionic transport in inorganic perovskite and ultrastable Cs-based perovskite solar cells. *J. Phys. Chem. Lett.* **8**, 4122-4128 (2017).

29 Kubicki, D. J., Stranks, S. D., Grey, C. P. & Emsley, L. NMR spectroscopy probes microstructure, dynamics and doping of metal halide perovskites. *Nat. Rev. Chem.* **5**, 624-645 (2021).

30 Kubicki, D. J. *et al.* Phase segregation in Cs-, Rb- and K-doped mixed-cation $(MA)_x(FA)_{1-x}PbI_3$ hybrid perovskites from solid-state NMR. *J. Am. Chem. Soc.* **139**, 14173-14180 (2017).

31 Xiao, J. W. *et al.* Stabilizing $RbPbBr_3$ perovskite nanocrystals through Cs^+ substitution. *Chem. Eur. J* **25**, 2597-2603 (2019).

32 Stoumpos, C. C. & Kanatzidis, M. G. The renaissance of halide perovskites and their evolution as emerging semiconductors. *Acc. Chem. Res.* **48**, 2791-2802 (2015).

33 Linaburg, M. R., McClure, E. T., Majher, J. D. & Woodward, P. M. $Cs_{1-x}Rb_xPbCl_3$ and $Cs_{1-x}Rb_xPbBr_3$ solid solutions: understanding octahedral tilting in lead halide perovskites. *Chem. Mater.* **29**, 3507-3514 (2017).

34 Deng, Y. *et al.* Defect compensation in formamidinium–caesium perovskites for highly efficient solar mini-modules with improved photostability. *Nat. Energy*

6, 633-641 (2021).

35 Eames, C. *et al.* Ionic transport in hybrid lead iodide perovskite solar cells. *Nat. Commun.* **6**, 7497 (2015).

36 El-Hajje, G. *et al.* Quantification of spatial inhomogeneity in perovskite solar cells by hyperspectral luminescence imaging. *Energy Environ. Sci.* **9**, 2286-2294 (2016).

37 Subedi, B. *et al.* Urbach energy and open-circuit voltage deficit for mixed anion-cation perovskite solar cells. *ACS Appl. Mater. Interfaces* **14**, 7796-7804 (2022).

38 Mahesh, S. *et al.* Revealing the origin of voltage loss in mixed-halide perovskite solar cells. *Energy Environ. Sci.* **13**, 258-267 (2020).

Fig. 1 | Properties of Rb/Cs mixed-cation inorganic perovskites. a, Schematic illustration of the suppression mechanism of LIPS. The hollow circles denote vacancies. **b**, **c**, UV-Vis absorption spectra and XRD patterns of $Rb_xCs_{1-x}PbI_{1.75}Br_{1.25}$ (x = 0, 0.05, 0.1, 0.15, 0.2). **d**, ^{133}Cs and ^{87}Rb solid-state MAS NMR spectra of Rb-doped cesium lead halides recorded at 20 T, 20 kHz MAS and room temperature. The green, purple, and blue lines represent pure-I, pure-Br, and mixed-I/Br phases. The δ and γ symbols indicate the hexagonal non-perovskite and 3D perovskite polymorphs, respectively. The light grey captions indicate secondary phases coexisting in small quantities with the main phase. Asterisks indicate spinning sidebands. **e**, The V_{OC} as a function of Rb doping content for the single-junction solar cells of $Rb_xCs_{1-x}PbI_2Br$, $Rb_xCs_{1-x}PbI_{1.75}Br_{1.25}$, and $Rb_xCs_{1-x}PbI_{1.5}Br_{1.5}$. **f**, The DFT-calculated Helmholtz free

energy ΔF (can be treated as a thermodynamic driving force) with different Rb doping content in $Rb_xCs_{1-x}PbI_{1.4}Br_{1.6}$ and $Rb_xCs_{1-x}PbI_{1.75}Br_{1.25}$ (see Methods for details).

Fig. 2 | The phenomena and mechanism of suppressed LIPS. a-c, PL spectra of $CsPbI_{1.4}Br_{1.6}$, $CsPbI_{1.75}Br_{1.25}$ and $Rb_{0.15}Cs_{0.85}PbI_{1.75}Br_{1.25}$ perovskite films under 1-sun AM 1.5G illumination for 60 minutes, respectively. **d**, **e**, The structures of the crystals from the loading compositions $CsPbI_{1.4}Br_{1.6}$ & $CsPbI_{1.75}Br_{1.25}$ (**d**) and $Rb_{0.15}Cs_{0.85}PbI_{1.75}Br_{1.25}$ (**e**) as viewed down the crystallographic *b*-axis. The halide positions are labeled by X (X = I/Br), and the labeling scheme for the atoms is consistent between the two structures. The Rb, Cs, Pb, I, and Br atoms are labeled in blue, yellow, grey, pink, and green, respectively. The fractional occupancy of the halide sites is shown as partially filled sectors. Halide sites X1–X4 propagate in the *a*-*c* plane, and halide sites X5–X8 propagate down the *b*-axis. **f**, **g**, Transient ion-migration currents (**f**) and calculated mobile ion concentrations (**g**) of $CsPbI_{1.4}Br_{1.6}$, $CsPbI_{1.75}Br_{1.25}$ and $Rb_{0.15}Cs_{0.85}PbI_{1.75}Br_{1.25}$ PSCs. **h-j**, DFT-calculated average ∠Pb–X–Pb (X = I, Br) (**h**), average A···X interatomic distance (**i**), and ion migration energy barrier of I (or Br) to V_I (or V_{Br}) (**j**) for $CsPbI_{1.4}Br_{1.6}$, $CsPbI_{1.75}Br_{1.25}$, and $Rb_{0.15}Cs_{0.85}PbI_{1.75}Br_{1.25}$. The arrows represent their trends. For $Rb_{0.15}Cs_{0.85}PbI_{1.75}Br_{1.25}$, the information around the Rb atoms is labeled with stars. Due to the supercell limitations, the real compositions used in calculations are $CsPbI_{1.375}Br_{1.625}$ (for $CsPbI_{1.4}Br_{1.6}$), $CsPbI_{1.75}Br_{1.25}$ (for $CsPbI_{1.75}Br_{1.25}$), and $Rb_{0.125}Cs_{0.875}PbI_{1.75}Br_{1.25}$ (for $Rb_{0.15}Cs_{0.85}PbI_{1.75}Br_{1.25}$).

Fig. 3 | PV performance of 2.0 eV single-junction PSCs. a, **b**, *J*-*V* curves and SPO of ~2.0 eV $CsPbI_{1.4}Br_{1.6}$ and $Rb_{0.15}Cs_{0.85}PbI_{1.75}Br_{1.25}$ PSCs. **c**, Statistics of PCE, V_{OC},

short-circuit current (J_{SC}), and fill factor (FF) of the $CsPbI_{1.4}Br_{1.6}$ devices (41 samples) and the $Rb_{0.15}Cs_{0.85}PbI_{1.75}Br_{1.25}$ devices (54 samples). **d**, Histogram of QFLS pixel values of $CsPbI_{1.4}Br_{1.6}$, and $Rb_{0.15}Cs_{0.85}PbI_{1.75}Br_{1.25}$ perovskites taken from larger 100 μm x 100 μm images. **e**, Near-Eg absorption coefficient (α) spectra from PDS for $CsPbI_{1.4}Br_{1.6}$ and $Rb_{0.15}Cs_{0.85}PbI_{1.75}Br_{1.25}$ thin films. Inset is Urbach energy extracted from the PDS measurements.

Fig. 4 | PV performance and stability of all-perovskite TJSCs. a, Schematic diagram of device structure and corresponding cross-sectional SEM image of the all-perovskite TJSC. The scale bar is 400 nm. **b**, *J-V* curves of reverse and forward scans for a champion all-perovskite TJSC. The *J-V* performances of the single-junction cells in all-perovskite triple-junction solar cells based on Ag electrodes are shown in **Supplementary Table 10**. **c**, NREL-certified QSS *J-V* curve of the all-perovskite triple-junction device. **d**, EQE curves of the ~2.0 eV, ~1.6 eV and ~1.22 eV subcells within the TJSC. **e**, The maximum power point stability tracking of an encapsulated TJSC at room temperature under simulated AM1.5G 1-sun illumination.

Materials and Methods

Materials

All materials were used as received without further purification. Lead iodide (PbI_2, 99.99%), lead bromide ($PbBr_2$, 99.999%), and [4-(3,6-Dimethyl-9H-carbazol-9-yl)butyl]phosphonic Acid (Me-4PACz) were purchased from TCI chemicals. Cesium iodide (CsI, 99.999%), Cesium bromide (CsBr, >99.9%), rubidium bromide (RbBr,

427 99.6%), tin (II) iodide (SnI_2, 99.99%, Beads), tin (II) fluoride (SnF_2, 99%), glycine
428 hydrochloride (99%), guanidine thiocyanate (GuaSCN, 99%), ethane-1,2-diammonium
429 iodide ($EDAI_2$ 98%), Polyethyleneimine, 80% ethoxylated solution (PEIE, 37 wt% in
430 water), nickel(ii) nitrate hexahydrate ($Ni(NO_3)_2 \cdot 6H_2O$, 99.999%) and sodium
431 hydroxide (NaOH, ≥99.99%) were purchased from Sigma-Aldrich. Methylammonium
432 iodide (MAI), formamidinium iodide (FAI), formamidinium chloride (FACl) and
433 phenethylammonium iodide (PEAI) were purchased from GreatCell Solar Materials.
434 Phenyl C61 Butyric Acid Methyl Ester (PCBM, 99.5%) and C_{60} were purchased from
435 Nano-C. Tetrakis(dimethylamino) tin (iv) (99.99%-Sn, 50-1815 Tin) was purchased
436 from Strem Chemicals.

437 Dimethyl sulfoxide (DMSO, 99.9%), N,N-dimethylformamide (DMF, 99.8%), 2-
438 propanol (IPA, 99.5%), chlorobenzene (CB, 99.8%), anisole (99.7%) and 1-propanol
439 (99.7%) were purchased from Sigma-Aldrich. Toluene (99.8%) was purchased from
440 Alfa Aesar. Poly(3,4-ethylenedioxythiophene) polystyrene sulfonate aqueous
441 solution ((PEDOT: PSS, Al-4083) was purchased from Ossila. Commercial ITO
442 substrates (20 Ω/sq) with 25 mm x 25 mm dimension were purchased from TFD Inc.
443 Quartz substrates were purchased from Shenzhen Weina Technology Electronic Co.
444 Ltd.

445 Preparation of inorganic perovskite precursor solutions

446 The precursor chemicals were mixed stoichiometrically with anhydrous dimethyl
447 sulfoxide solvent and stirred until completely dissolved. Before used, the perovskite

precursor solution was filtered through a 0.22 μm polytetrafluoroethylene (PTFE) membrane.

FACl (FACl:Pb^{2+} = 0.1 mmol:1 mmol) was added into the I/Br mixed precursor solutions as an additive to improve the interfacial contact of inorganic perovskite and substrate[39]. FACl was evaporated during the annealing process at 180 ºC (**Supplementary Fig. 9)**[40]. For simplicity, we did not show the 0.1 mmol FACl additive and 1 ml DMSO in the following recipes.

1 M $Rb_{0.15}Cs_{0.85}PbI_{1.75}Br_{1.25}$ = 0.15 mmol RbI + 0.85 mmol CsI + 0.375 mmol PbI_2 + 0.625 mmol $PbBr_2$

1 M $CsPbI_{1.4}Br_{1.6}$ = 1 mmol CsI + 0.2 mmol PbI_2 + 0.8 mmol $PbBr_2$

1 M $CsPbI_{1.75}Br_{1.25}$ = 1 mmol CsI + 0.375 mmol PbI_2 + 0.625 mmol $PbBr_2$

1 M $RbPbI_{1.75}Br_{1.25}$ = 1 mmol RbI + 0.375 mmol PbI_2 + 0.625 mmol $PbBr_2$

1M $CsPbI_2Br$ = 1 mmol CsI + 0. 5 mmol PbI_2 + 0.5 mmol $PbBr_2$

1M $RbPbI_2Br$ = 1 mmol RbI + 0. 5 mmol PbI_2 + 0.5 mmol $PbBr_2$

1M $CsPbI_{1.5}Br_{1.5}$ = 1 mmol CsI + 0. 25 mmol PbI_2 + 0.75 mmol $PbBr_2$

1M $RbPbI_{1.5}Br_{1.5}$ = 1 mmol RbI + 0. 25 mmol PbI_2 + 0.75 mmol $PbBr_2$

For pure Br precursor solutions, the concentration is 0.5 M without additives because 1 M cannot be dissolved in DMSO.

0.5 M $CsPbBr_3$ = 0.5 mmol CsBr + 0.5 mmol $PbBr_2$

0.5 M $RbPbBr_3$ = 0.5 mmol RbBr + 0.5 mmol $PbBr_2$

DMAI (DMAI:Pb^{2+} = 1 mmol:1 mmol) is added into the following pure-I precursor solutions as an additive to promote the formation of pure-I inorganic perovskites[41]. DMAI was evaporated during the annealing process at 250 ºC[42]. For simplicity, we did not show the 1 mmol DMAI additive and 1 ml DMSO in the following recipes.

1M $CsPbI_3$ = 1 mmol CsI + 1 mmol PbI_2

1M $RbPbI_3$ = 1 mmol RbI + 1 mmol PbI_2

$Rb_xCs_{1-x}PbX_3$ (X = I, Br) precursor solutions can be obtained by mixing the $CsPbX_3$ and $RbPbX_3$ precursor solutions based on volume ratios.

Nickel oxide nanoparticle synthesis

The NiO_x nanoparticles were prepared via the hydrolysis of nickel nitrate following previous work[43]. Briefly, $Ni(NO_3)_2 \cdot 6H_2O$ (20 mmol) was dissolved in deionized water (20 ml) to obtain a dark-green solution. Then, NaOH aqueous solution (4 ml, 10 M) was slowly added to the dark-green solution with stirring. After being stirred for 20 minutes, the colloidal precipitate was washed thoroughly using deionized water three times and dried at 80 °C for 6 hours. The obtained green powder was then calcined at 270 °C for 2 hours to obtain a black powder. The NiO_x nanoparticle ink was prepared by dispersing the obtained NiO_x nanoparticles in a mixed solution of deionized water and IPA (3:1, v/v) for a concentration of 5mg/ml.

Inorganic perovskite device fabrication

The configuration of inorganic perovskite devices is ITO glass/NiO_x/Me-4PACz/Inorganic perovskite/ PEAI-$EDAI_2$/PCBM/PEIE/SnO_x/Ag.

1. ITO glass. The pre-patterned ITO glasses were sequentially sonicated in acetone and IPA each for 20 minutes. After drying with nitrogen, the substrates were exposed to UV-ozone treatment for 20 minutes to remove organic contaminants.

2. NiO_x layer. NiO_x layers were prepared by spin-coating 100 μL NiO_x nanoparticle solution on ITO substrates at 3,000 rpm for 25 s in the air without any post-treatment, then immediately transferred to a nitrogen-filled glovebox.

3. Me-4PACz layer. 100 μL Me-4PACz (0.5 mg/ml) solution in ethanol was spin-coated on the NiO_x film at 3,000 rpm for 30 s in a nitrogen-filled glovebox. Then the prepared film was annealed at 100 °C for 10 minutes.

4. Inorganic perovskite layer. For Br-based or I-Br mixed perovskite films, 100 μL inorganic perovskite precursor solution was spin-coated on the substrate at 3,000 rpm for 70 s. The film was firstly annealed at 40 °C until the color of the film started to turn brown (5–20 s in our lab), then quickly moved to a 180 °C hotplate for five-minute annealing.

For pure I-based inorganic perovskite, 100 μL inorganic perovskite precursor solution was spin-coated on the substrate at 3,000 rpm for 70 s. Then the film was annealed at 250 °C for 5 minutes.

5. PEAI-$EDAI_2$ modified layer. The treatment solution was prepared by dissolving 1 mg PEAI and 1 mg $EDAI_2$ into 1 ml IPA. 130 μL filtered solution was spin-coated on the inorganic perovskite film at 4,000 rpm for 25 s. Then the film was annealed at 100 °C for 5 minutes.

6. PCBM layers. 70 μL PCBM (15 mg/ml) solution in CB was spin-coated on the inorganic perovskite/PEAI-$EDAI_2$ film at 1,000 rpm for 30 s.

7. PEIE layers. 100 μL PEIE (0.025 wt%) solution in IPA was spin-coated on the PCBM film at 4,000 rpm for 30 s.

8. SnO_x layer. The film was then transferred to the atomic layer deposition (ALD) system (Picosun) to deposit 20 nm SnO_x at 100 ºC using precursors of tetrakis(dimethylamino) tin (iv) (99.9999%) and deionized water.

9. Ag electrode. 140-nm-thick Ag electrode was deposited by thermal evaporation.

Fabrication of all-perovskite triple-junction solar cells

The configuration of the triple-junction solar cells is ITO/NiO_x/Me-4PACz/2.0 eV inorganic perovskite (170nm)/PEAI-$EDAI_2$/PCBM/PEIE/SnO_x/ITO/NiO_x/Me-4PACz/1.6 eV perovskite (780nm)/PEAI-$EDAI_2$/PCBM/PEIE/SnO_x/Au/PEDOT:PSS/1.22 eV SnPb perovskite (870 nm)/C_{60}/SnO_x/Ag.

1. ~ 2.0 eV inorganic perovskite top cell. The fabrications of ITO glass, NiO_x, Me-4PACz, PEAI-$EDAI_2$, PCBM, PEIE, and SnO_x layers are the same as inorganic perovskite single-junction devices. The PEIE layer can increase the compatibility of SnO_x, which can protect the perovskite layer from degradation when spin-coating the following NiO_x and perovskite layers[44]. For 2.0 eV inorganic perovskite layers, 100 μL 0.8 M $Rb_{0.15}Cs_{0.85}PbI_{1.75}Br_{1.25}$ inorganic perovskite precursor solution was spin-coated

on the substrate at 3,000 rpm for 70 s. The film was firstly annealed at 40 °C for 15 s, then quickly moved to a 180 °C hotplate for 5 minutes.

2. ITO layer. The top cell was then transferred to the radio-frequency magnetron sputtering system. The ITO target used in this study is a commercial grade of purity of >99.99% with a size of 3.00" Dia x 0.125" Thick. The target composition is In_2O_3/SnO_2 90/10 wt%. The process pressure is 3 mTorr at Ar flow of 18 sccm. The average deposition rate is about 0.24A/s at 33 W power. A total ITO layer thickness of 20 nm is deposited.

3. ~ 1.6 eV perovskite middle cell. The fabrication procedures of the NiO_x, Me-4PACz, PEAI-$EDAI_2$, PCBM, PEIE, and SnO_x layers are very similar to those described above for the single-junction inorganic perovskite devices. The only difference is that the subcell was treated by plasma etching for 30s to increase its surface wettability before spin-coating the NiO_x nanoparticle solution. For the 1.6 eV perovskite film, the $Cs_{0.05}FA_{0.9}MA_{0.05}Pb(I_{0.9}Br_{0.1})_3$ perovskite precursor solution (1.5 M) was prepared by dissolving 0.075 mmol CsI, 0.075 mmol MABr, 1.35 mmol FAI, 0.1875 mmol $PbBr_2$, and 1.3125 mmol PbI_2 in a mixed solvent of DMF and DMSO with a volume ratio of 4:1. The perovskite precursor solution was filtered through a 0.22 μm PTFE membrane before use. 100 μL of perovskite solution was dropped on the substrate and spin-coated at 1000 rpm for 10 s followed by 5000 rpm for 30 s. 150 μL anisole was dropped onto the substrate at the last 5 s of the spin-coating, resulting in the formation of dark brown films that were then annealed on a hot plate at 100°C for 10 minutes.

4. Au layer. A 1-nm-thick Au electrode was deposited by thermal evaporation.

552 5. ~ 1.22 eV SnPb perovskite bottom cell. The PEDOT:PSS layer was prepared by spin-
553 coating 100 μL diluted PEDOT:PSS solution with n-propanol at a volume ratio of 1:1
554 on the substrate at 4,000 rpm for 30 s and then annealing at 100 °C for 15 minutes in
555 ambient air. After cooling, we immediately transferred the substrates to a nitrogen-filled
556 glovebox to deposit perovskite films. 1.8 M SnPb perovskite precursor solution with a
557 composition of $Cs_{0.05}FA_{0.7}MA_{0.25}Pb_{0.5}Sn_{0.5}I_3-0.05SnF_2$ was prepared by dissolving 0.09
558 mmol CsI, 1.26 mmol FAI, 0.45mmol MAI, 0.9 mmol SnI_2, 0.9mmol PbI_2 and 0.09
559 mmol SnF_2 in a 1 ml mixed solvent of DMF and DMSO with a volume ratio of 3:1. Tin
560 powders (5 mg), GuaSCN (4 mg), 4F-PEABr (2 mg) and glycine hydrochloride (4 mg)
561 were added to the precursor solution. The precursor solution was then stirred at room
562 temperature for 1 hour. The precursor solution was filtered using a 0.22 μm PTFE
563 membrane before deposition. 70 μL of perovskite solution was deposited on the
564 substrate and spin-coated with a two-step spin-coating procedure: 1000 rpm for 10 s
565 and 3800 rpm for 45 s. 300 μl CB was dropped onto the substrate during the second
566 spin-coating step at the last 20 s of the spin-coating. The substrates were then annealed
567 at 100 °C for 10 minutes. 20 nm C_{60}, 20 nm SnO_x, and 140nm Ag were sequentially
568 deposited on the top of SnPb perovskite layer by organic thermal evaporation, ALD,
569 and metal thermal evaporation, respectively.

570 **Additional References:**

571 39 Zhang, J. *et al.* Intermediate phase enhances inorganic perovskite and metal
572 oxide interface for efficient photovoltaics. *Joule* **4**, 222-234 (2020).

573 40 Wang, Z. *et al.* Additive-modulated evolution of $HC(NH_2)_2PbI_3$ black

polymorph for mesoscopic perovskite solar cells. *Chem. Mater.* **27**, 7149-7155 (2015).

41 Wang, Y. *et al.* Thermodynamically stabilized β-$CsPbI_3$-based perovskite solar cells with efficiencies >18%. *Science*, 591-595 (2019).

42 Meng, H. *et al.* Chemical composition and phase evolution in DMAI-derived inorganic perovskite solar cells. *ACS Energy Lett.* **5**, 263-270 (2019).

43 Chen, H. *et al.* Quantum-size-tuned heterostructures enable efficient and stable inverted perovskite solar cells. *Nat. Photonics* **16**, 352-358 (2022).

44 Palmstrom, A. F. *et al.* Enabling flexible all-perovskite tandem solar cells. *Joule* **3**, 2193-2204 (2019).

Acknowledgments

This research was made possible by the US Department of the Navy, Office of Naval Research Grant (N00014-20-1-2572), the U.S. Department of Energy's Office of Energy Efficiency and Renewable Energy (EERE) under the Solar Energy Technologies Office Award Number DE-EE0008753. This work was supported in part by the Ontario Research Fund-Research Excellence program (ORF7-Ministry of Research and Innovation, Ontario Research Fund-Research Excellence Round 7). M.G.K. was supported by the Office of Naval Research (ONR) under grant N00014-20-1-2725. At King Abdullah University of Science and Technology (KAUST), this work was supported by the under Award No. OSR-CRG2020-4350.2. This work was also supported by the Natural Sciences and Engineering Council of Canada and the Vanier Canada Graduate Scholarship. Z.W. acknowledges the Banting Postdoctoral

Fellowships Program of Canada. D.J.K. acknowledges the support of the University of Warwick. The UK High-Field Solid-State NMR Facility used in this research was funded by EPSRC and BBSRC (EP/T015063/1), as well as the University of Warwick, including via part funding through Birmingham Science City Advanced Materials Projects 1 and 2 supported by Advantage West Midlands (AWM) and the European Regional Development Fund (ERDF). The crystallographic experiments made use of the IMSERC Crystallography and Physical Characterization facilities at Northwestern University, which received support from the Soft and Hybrid Nanotechnology Experimental (SHyNE) Resource (NSF ECCS-2025633), and Northwestern University. The purchase of the Ag-microsource used to collect both single and powder diffraction data was supported by the Major Research Instrumentation Program for the National Science Foundation under the award CHE-1920248. This work also made use of the EPIC facility at Northwestern University's NUANCE Center, which has received support from the SHyNE Resource (NSF ECCS-2025633), the IIN, and Northwestern's MRSEC program (NSF DMR-1720139). Computations were performed on the Niagara supercomputer at the SciNet HPC Consortium. SciNet is funded by the Canada Foundation for Innovation; the Government of Ontario; Ontario Research Fund Research Excellence; and the University of Toronto. A.B. was supported, in part, by a fellowship through the National Defense Science and Engineering Graduate (NDSEG) Fellowship Program, sponsored by the Air Force Research Laboratory (AFRL), the Office of Naval Research (ONR), and Army Research Office (ARO). We thank Dr. Tao Song for efficiency certification in NREL. Z.W. thanks Dr. Yicheng Zhao, Dr. Zhenyi

Ni and Dr. Emre Yengel for discussion about LIPS. A.B. acknowledges Dr. Christos D. Malliakas for assistance with the single crystal measurements and important discussions. A.B. also thanks Dr. Abishek K. Iyler, Craig Laing, and Michael Quintero for discussions.

Author Contributions:

Z.W. conceived the idea of this project. L.Z. and Z.W. fabricated the ~2.0 eV band gap devices and triple-junction solar cells for performance and fabricated the perovskite films for characterizations. H.C., L.Z, and Z.W. fabricated the ~1.6 eV band gap cells. L.Z., Z.W., A.M and C.L. fabricated the ~1.22 eV band gap cells. T.Z. carried out the DFT calculations and analyzed the data. H.C. prepared NiO_x nanoparticles and developed the surface passivation of the inorganic perovskite layers and 1.6 eV perovskite layers. B.C. helped with experimental design and data analysis. D.J.K. carried out the solid-state NMR characterization, prepared the corresponding powders and analyzed the data. A.B. prepared the crystals and carried out the crystal XRD and data analysis. C.L. carried out EQE measurements. E.U. carried out the PL mapping and QFLS analysis. R.R. and M.C. carried out the TEM-EDS and data analysis. G.Y. measured transient ion-migration currents and carried out data analysis. B.S. performed PDS characterizations and data analysis. D.L. and J.H. carried out the depth-profile XPS characterization and data analysis. S.W. carried out the AFM characterization. L.Z. and Z.W. carried out the UV-Vis measurements, XRD measurements, PL measurements, *JV* measurements, and stability measurements. Z.W. wrote the original draft. E.H.S., L.W., T.Z., D.J.K., and A.M., helped to review and edit the manuscript.

E.H.S. secured funding. All the authors contributed to the discussion of the results and the final manuscript preparation.

Ethics declarations

Competing Interests:

The authors declare no competing interests.

Data and Materials Availability:

All data are available in the main text or supplementary materials.

The crystallographic files (CIF) for the compounds reported in this work can be found as depositions in the Cambridge Crystallographic Data Centre (CCDC) based on the following deposition numbers: 2211086 – $CsPbI_{1.46}Br_{1.54}$, 2211087 – $CsPbI_{1.73}Br_{1.27}$, and 2211088 – $Rb_{0.22}Cs_{0.78}PbI_{1.65}Br_{1.35}$.

The codes and post-analysis tools for calculations are available from FHI-aims websites: https://fhi-aims.org/

Supplementary Information

Materials and Methods

Supplementary Figs. 1 to 25

Supplementary Tables 1 to 13

Supplementary Note 1 to 12

References

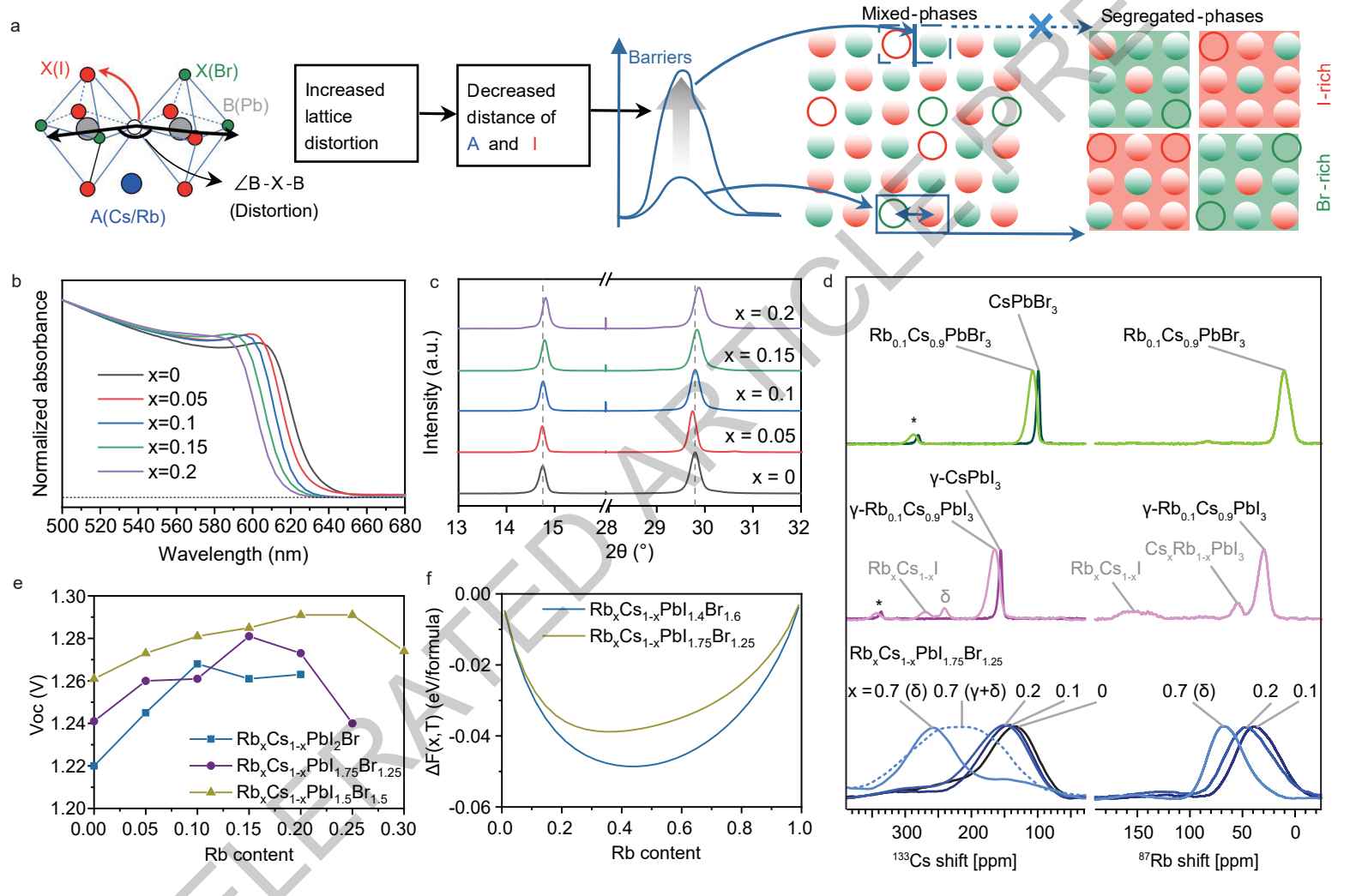

a

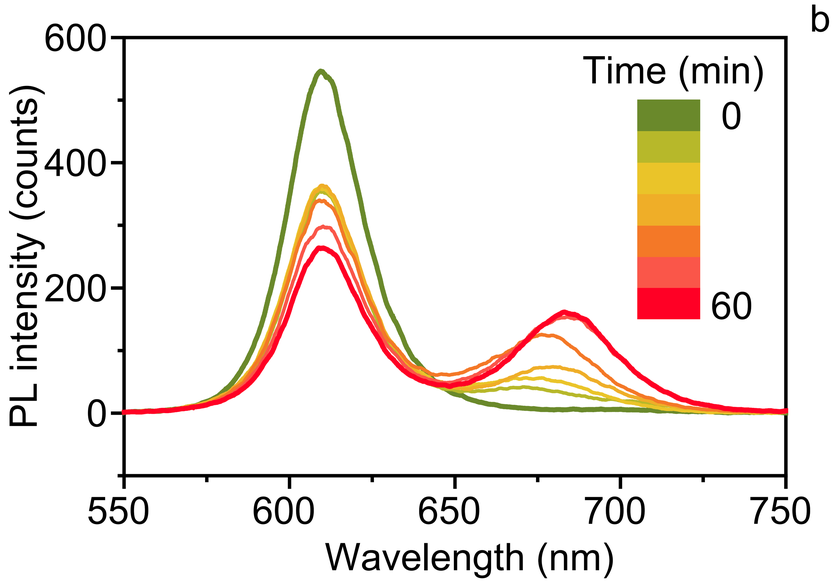

b

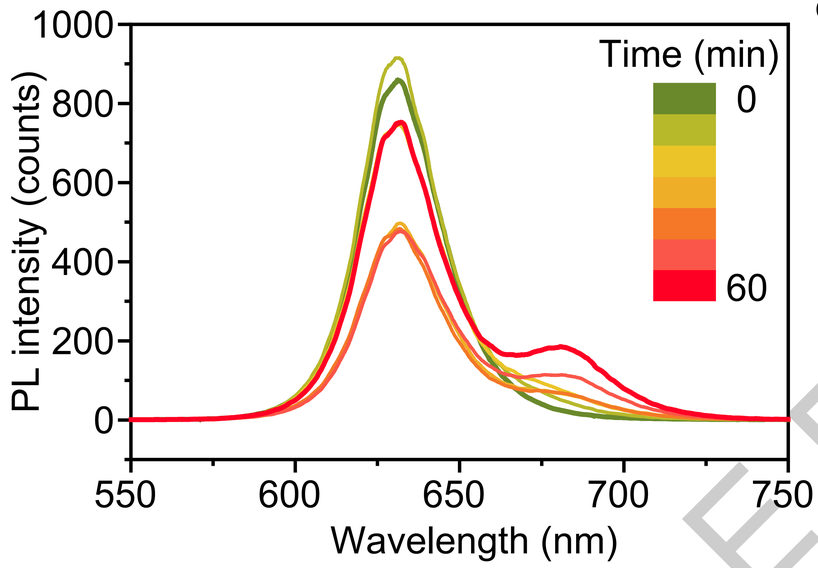

c

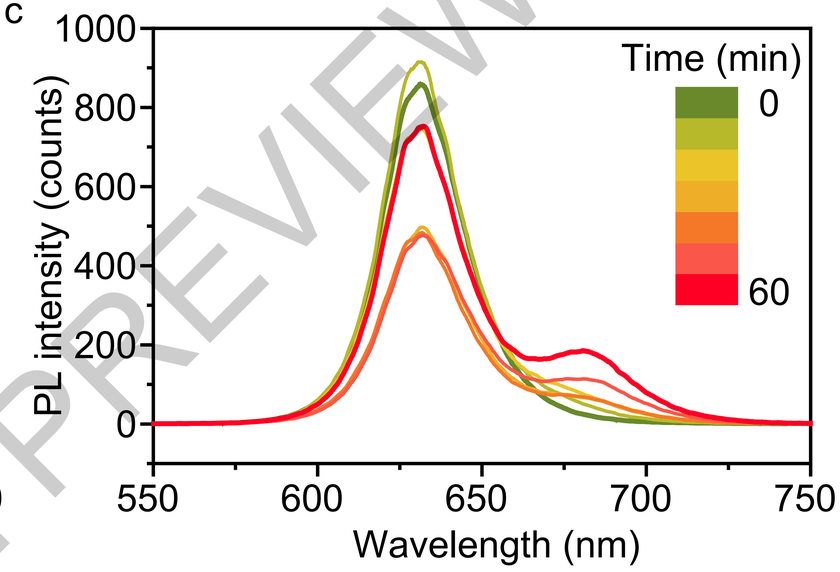

d

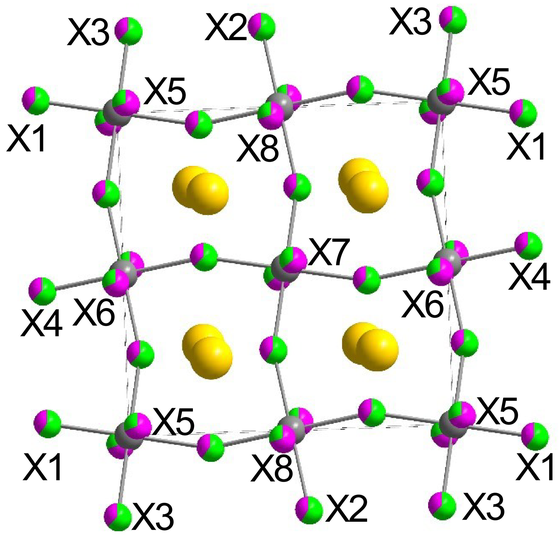

e

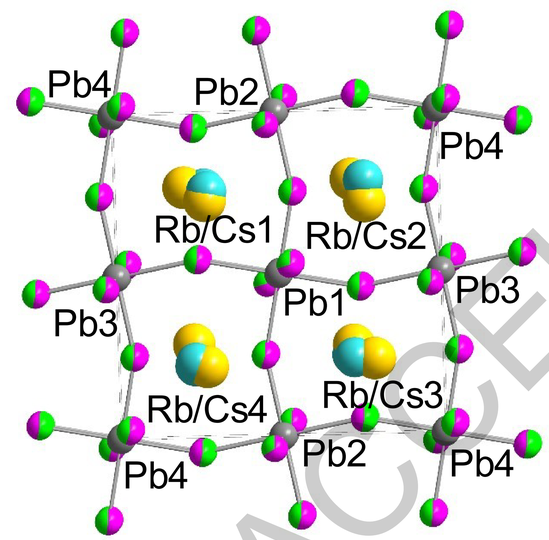

f

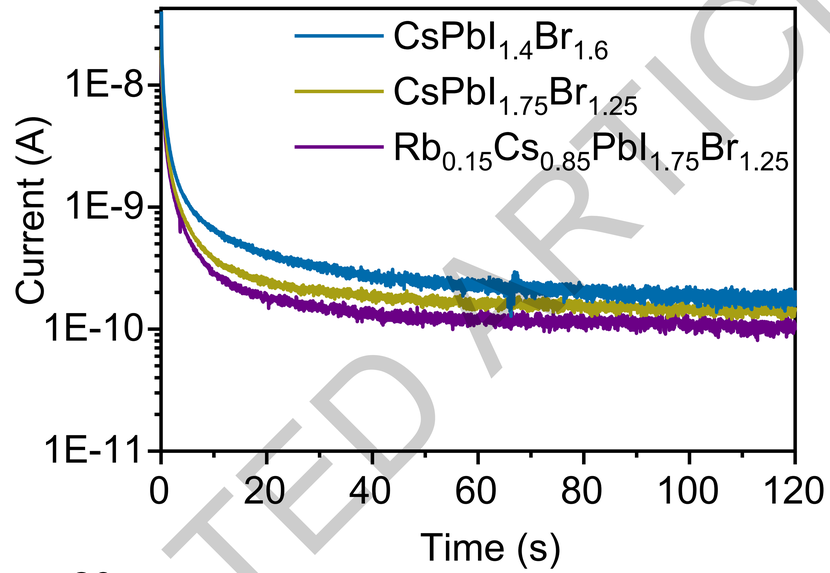

g

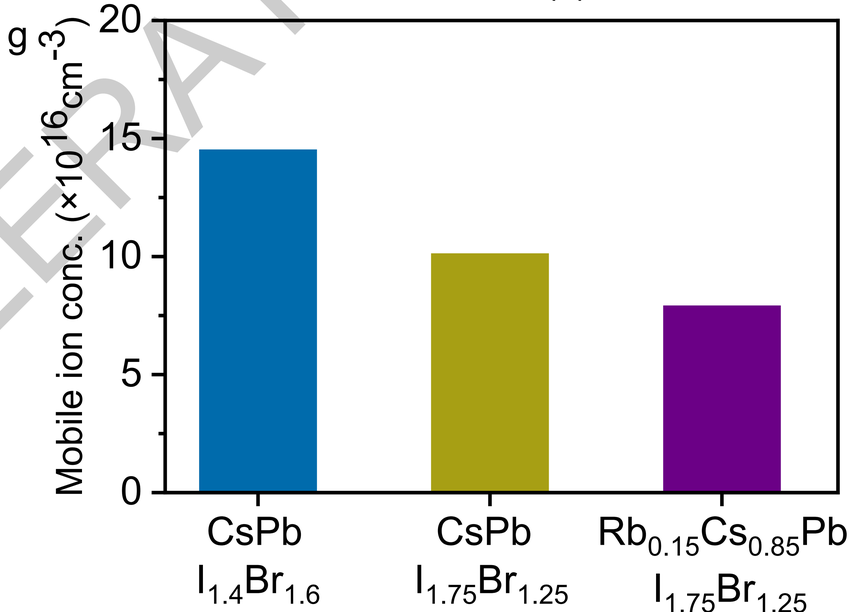

h

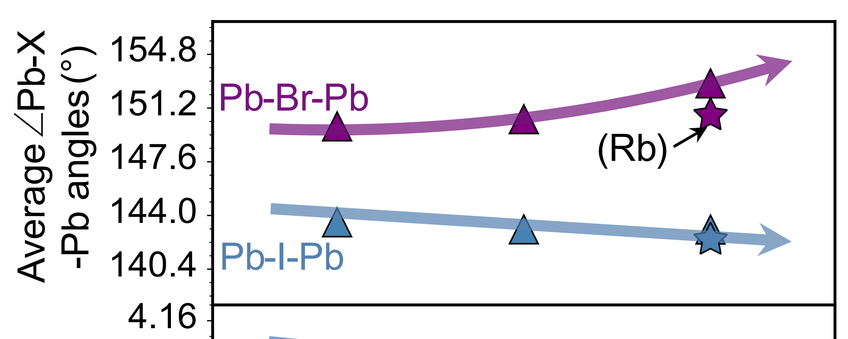

i

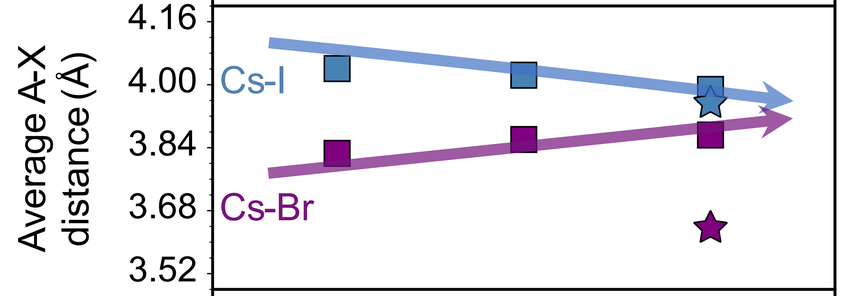

j

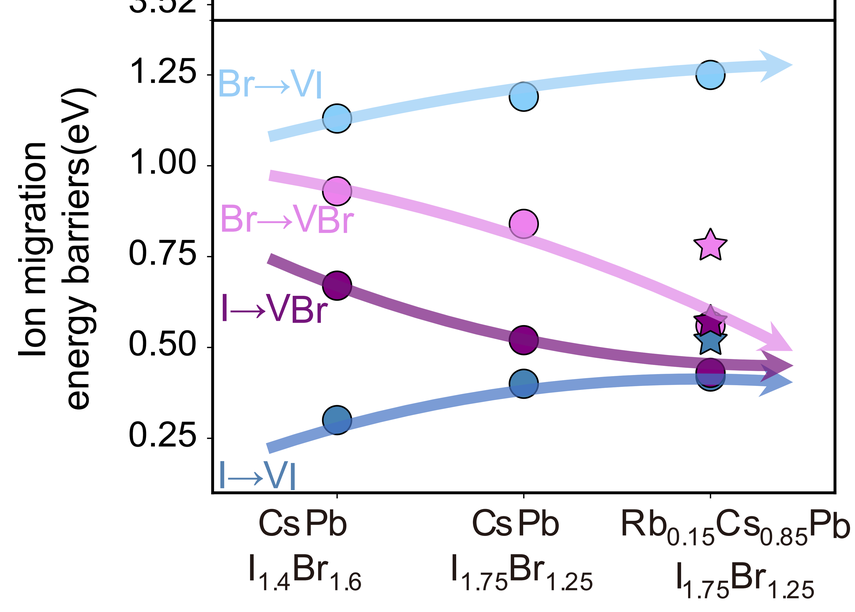

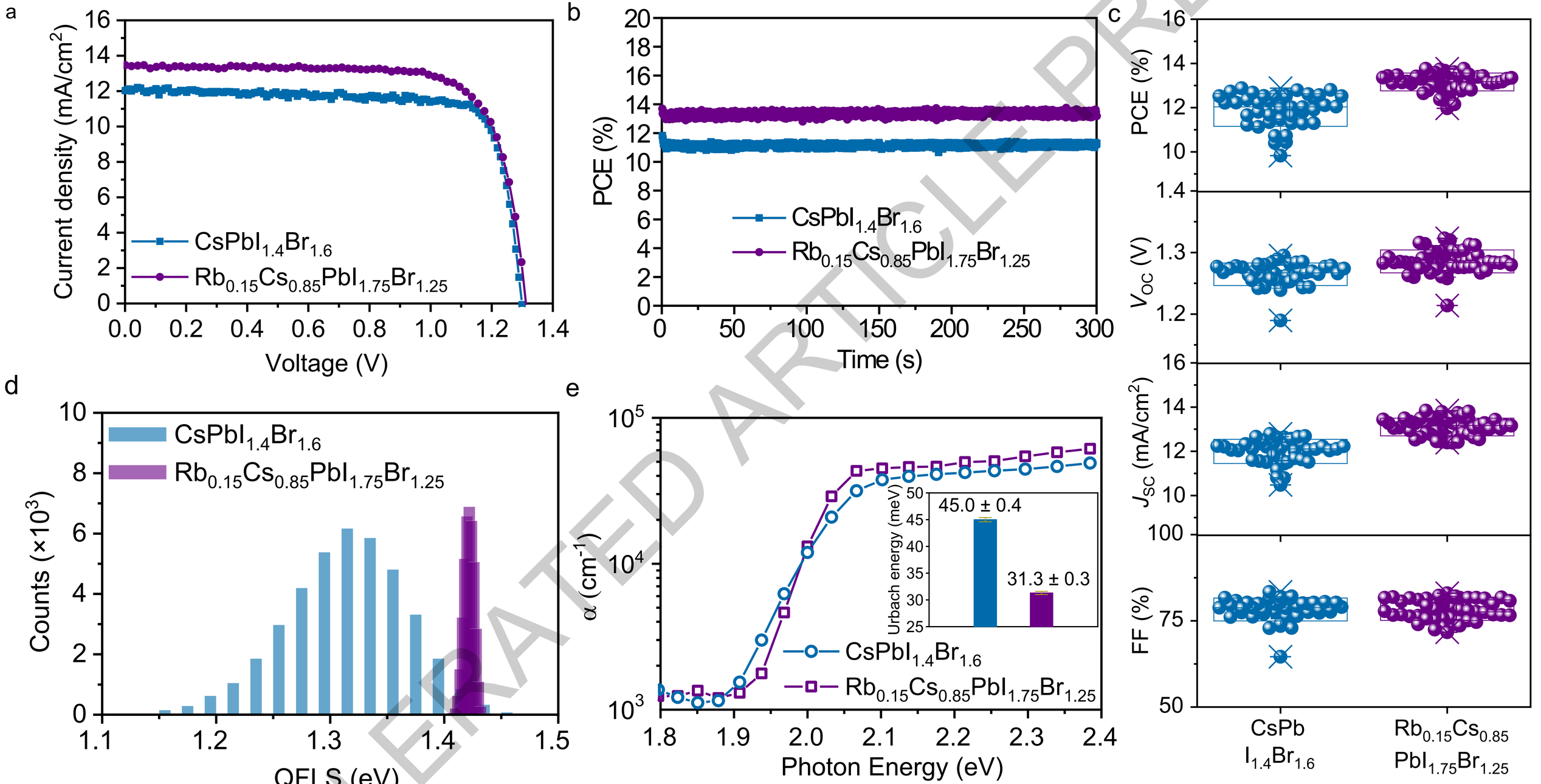

a

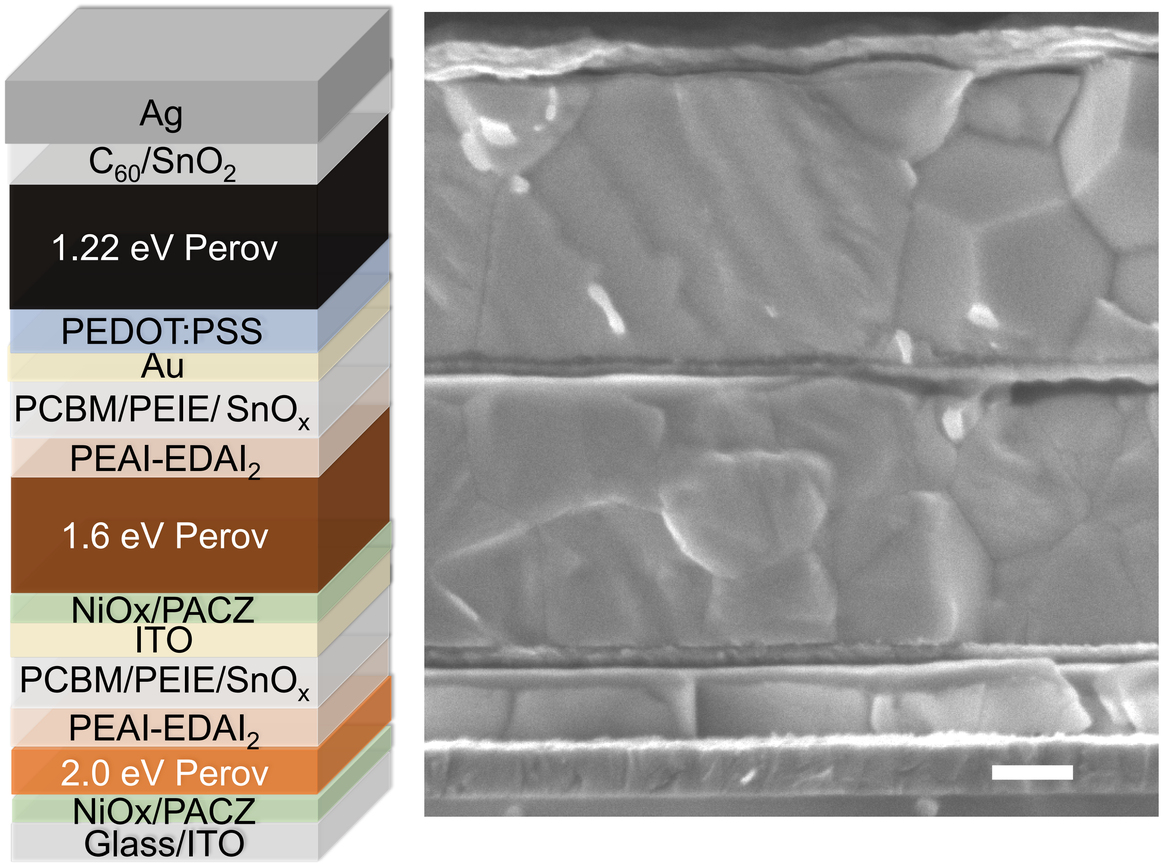

b

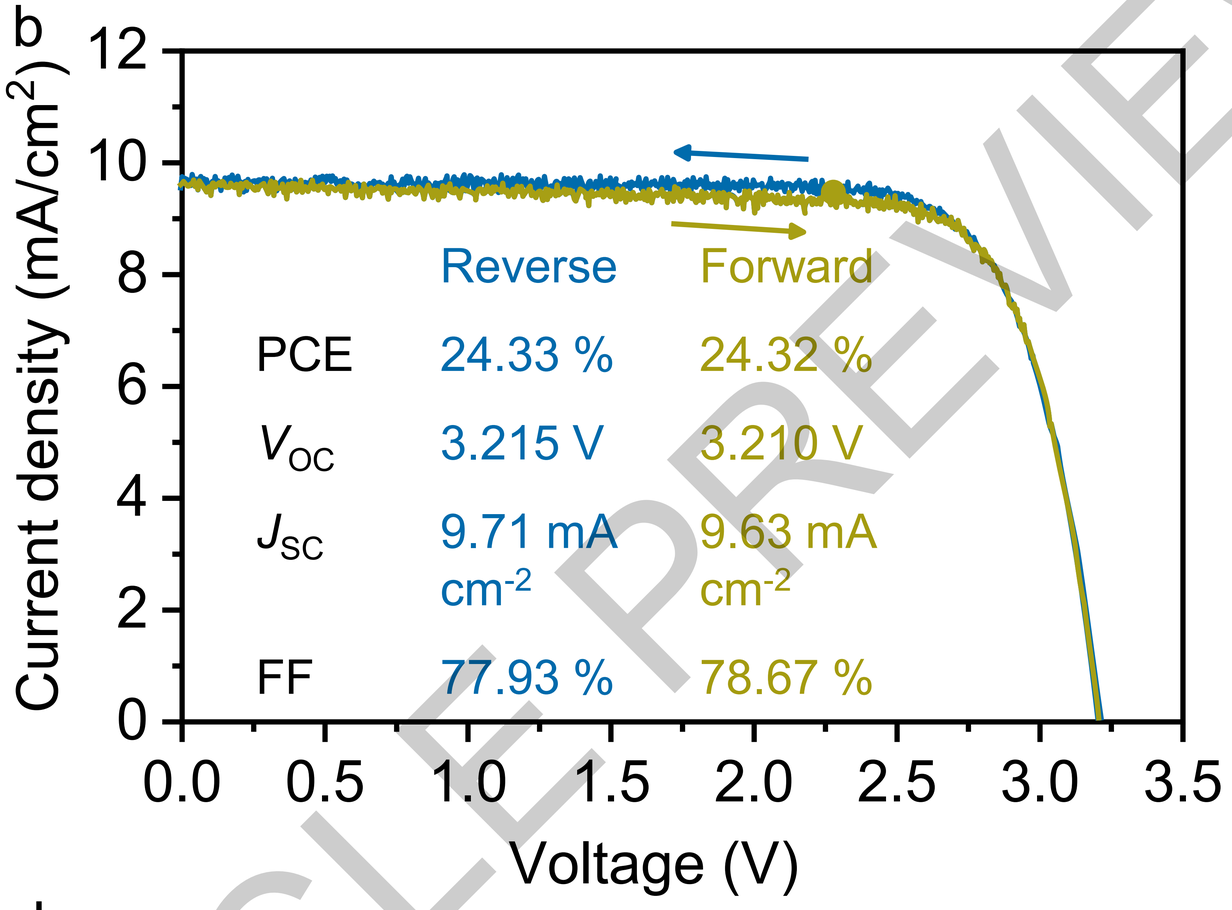

c

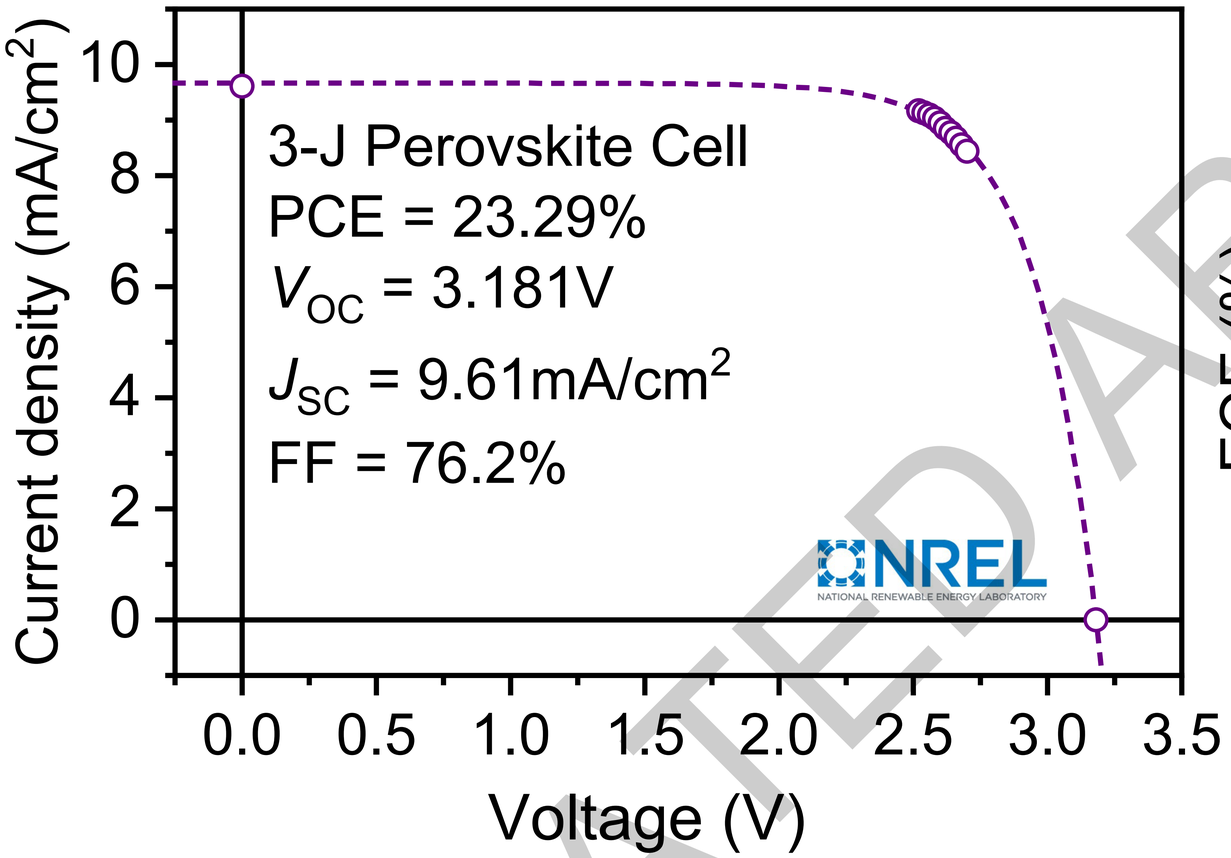

d

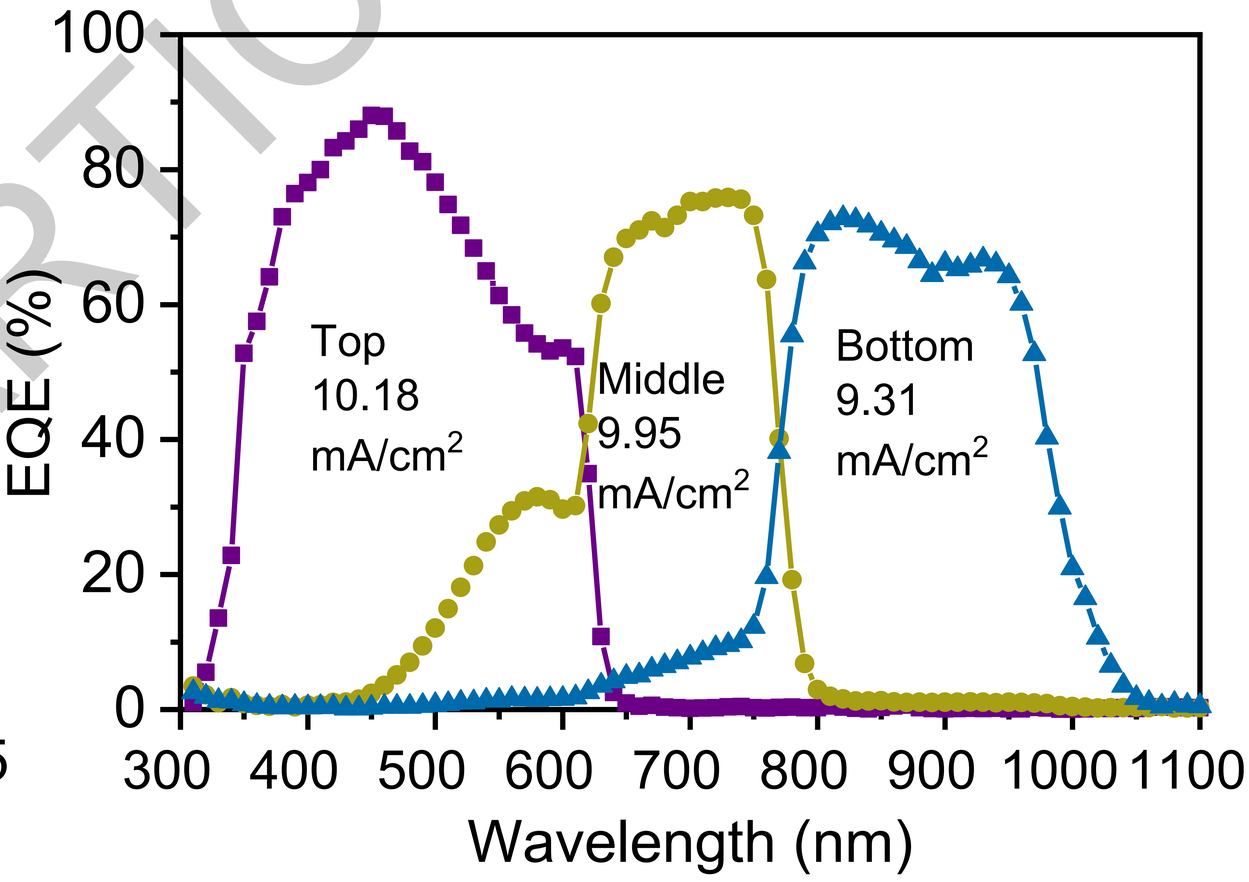

e

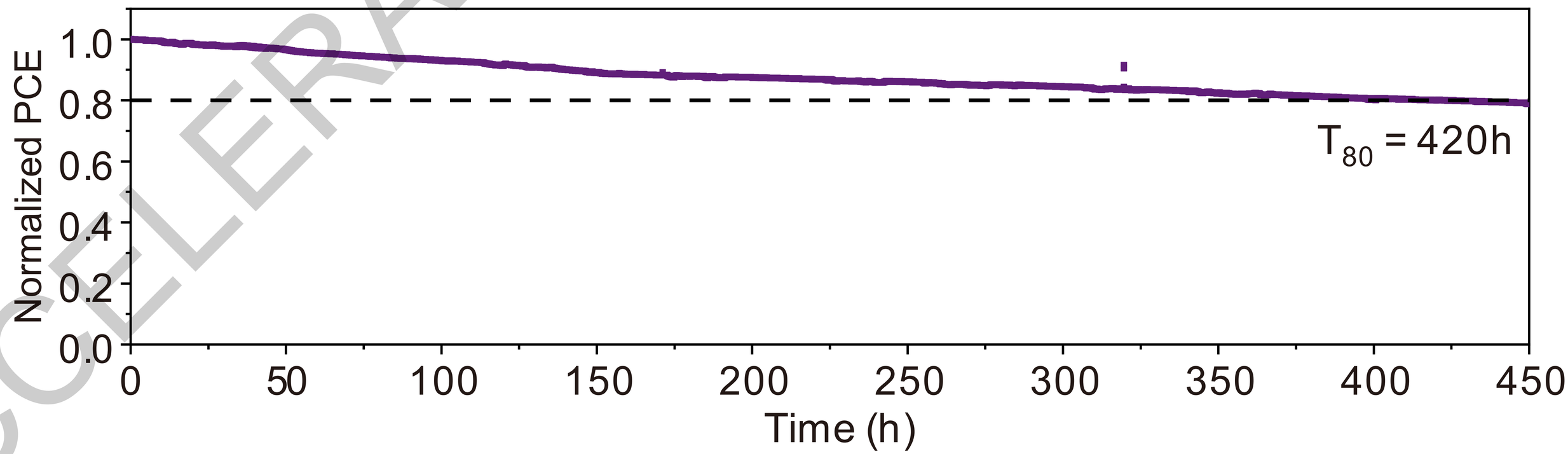

nature research

Corresponding author(s): Edward Sargent

Solar Cells Reporting Summary

Nature Research wishes to improve the reproducibility of the work that we publish. This form is intended for publication with all accepted papers reporting the characterization of photovoltaic devices and provides structure for consistency and transparency in reporting. Some list items might not apply to an individual manuscript, but all fields must be completed for clarity.

For further information on Nature Research policies, including our data availability policy, see Authors & Referees.

Experimental design

Please check: are the following details reported in the manuscript?

1. Dimensions

Area of the tested solar cells	☒ Yes ☐ No	Device testing in Methods
Method used to determine the device area	☒ Yes ☐ No	Device testing in Methods

2. Current-voltage characterization

Current density-voltage (J-V) plots in both forward and backward direction	☒ Yes ☐ No	Figure 4b & Supplementary Fig. 21
Voltage scan conditions *For instance: scan direction, speed, dwell times*	☒ Yes ☐ No	Figure 3a & 4b & Supplementary Fig. 21
Test environment *For instance: characterization temperature, in air or in glove box*	☒ Yes ☐ No	Device testing in Methods
Protocol for preconditioning of the device before its characterization	☒ Yes ☐ No	Solar cell fabrication and device testing in Methods
Stability of the J-V characteristic *Verified with time evolution of the maximum power point or with the photocurrent at maximum power point; see ref. 7 for details.*	☒ Yes ☐ No	Stability testing in Methods, Figure 4e & Supplementary Fig. 21

3. Hysteresis or any other unusual behaviour

Description of the unusual behaviour observed during the characterization	☐ Yes ☒ No	Negligible hysteresis
Related experimental data	☒ Yes ☐ No	Throughout main text and supplementary information

4. Efficiency

External quantum efficiency (EQE) or incident photons to current efficiency (IPCE)	☒ Yes ☐ No	Figure 4d
A comparison between the integrated response under the standard reference spectrum and the response measure under the simulator	☒ Yes ☐ No	Certified results in Figure 4c & supplementary figure 22
For tandem solar cells, the bias illumination and bias voltage used for each subcell	☒ Yes ☐ No	Device testing in methods

5. Calibration

Light source and reference cell or sensor used for the characterization	☒ Yes ☐ No	Device testing in methods
Confirmation that the reference cell was calibrated and certified	☒ Yes ☐ No	Device testing in methods

Calculation of spectral mismatch between the reference cell and the devices under test	☒ Yes ☐ No	Device testing in methods

6. Mask/aperture

Size of the mask/aperture used during testing	☒ Yes ☐ No	Device testing in methods
Variation of the measured short-circuit current density with the mask/aperture area	☒ Yes ☐ No	Figure 3a, 4b, Supplementary Figure 21, 25

7. Performance certification

Identity of the independent certification laboratory that confirmed the photovoltaic performance	☒ Yes ☐ No	Main text, Figure 4c , Supplementary Figure 21
A copy of any certificate(s) *Provide in Supplementary Information*	☒ Yes ☐ No	Supplementary Figure 22

8. Statistics

Number of solar cells tested	☒ Yes ☐ No	Figure 3c, Supplementary Figure 24
Statistical analysis of the device performance	☒ Yes ☐ No	Figure 3c, Supplementary Figure 24

9. Long-term stability analysis

Type of analysis, bias conditions and environmental conditions *For instance: illumination type, temperature, atmosphere humidity, encapsulation method, preconditioning temperature*	☒ Yes ☐ No	Fig 4e, Supplementary Figure 21 and 23, 25. stability testing in methods